

REGULAR PAPER • OPEN ACCESS

A comparative simulation study on lateral and L-shaped PN junction phase shifters for single-drive 50 Gbps lumped Mach–Zehnder modulators

To cite this article: Younghyun Kim *et al* 2021 *Jpn. J. Appl. Phys.* **60** 052002

View the [article online](#) for updates and enhancements.



A comparative simulation study on lateral and L-shaped PN junction phase shifters for single-drive 50 Gbps lumped Mach–Zehnder modulators

Younghyun Kim^{*}, Taewon Jin, and Youngjoo Bae

Department of Photonics and Nanoelectronics, Hanyang University ERICA, Ansan, Gyeonggi-do 15588, Republic of Korea

^{*}E-mail: younghyunkim@hanyang.ac.kr

Received December 17, 2020; revised March 11, 2021; accepted March 14, 2021; published online April 20, 2021

We present a comparative study of lateral and L-shaped PN junction Si optical phase shifters for Mach–Zehnder modulators in Si photonics based on TCAD simulation. First, we introduce an easy fabrication method for L-shaped PN junctions by inverting dominant dopant type in Si. Then, we present the quantitative comparison of Si optical phase shifters. The L-shaped PN junction device shows the larger modulation efficiency of V_{piL} and the lower optical phase shifter loss compared to the lateral one. The V_{piL} for the vertical one is 0.89 Vcm, nearly half that of the lateral one, 1.76 Vcm at the same optical phase shifter loss, 10.5 dB cm⁻¹. Finally, taking advantage of single-drive configuration and optimizing input characteristic impedance, the large-signal simulation with 1 mW input power and a 500 μ m phase shifter shows the dynamic optical modulation amplitude of 0.22 mW for the vertical one, which could be a promising solution for a compact device footprint without a traveling wave electrode.

© 2021 The Japan Society of Applied Physics

1. Introduction

Depletion-type silicon (Si) Mach–Zehnder modulators (MZM) have been mostly used as a key building block for high-performance optical interconnect systems based on Si photonics because they can provide high modulation speed and broad bandwidths which are highly attractive for cost-effective co-integration of photonics and electronics.^{1–5} In particular, Si traveling wave MZMs have been actively investigated for the 200 Gb s⁻¹ and 400 Gb s⁻¹ IEEE Ethernet standards, taking advantage of four-level pulse amplitude modulation (PAM-4)⁶ and quadrature phase shift keying (QPSK).⁷

The Si optical phase shifters on the MZMs consist of a PN junction within Si rib waveguides, where the plasma dispersion effect occurs and changes the refractive index.^{8,9} In general, Si optical phase shifters based on PN junctions are classified as lateral PN junctions (LPNs) or L-shaped PN junctions (LSPNs). LPN-based optical phase shifters are the most commonly used due to their relatively easy fabrication and simple design. However, the modulation efficiency of the V_{piL} of Si optical phase shifters based on LPN is as high as 1.5 to 2.5 Vcm^{10–13} (the modulation efficiency of an optical phase shifter is characterized by the voltage–length product of a π phase shift; therefore, a small V_{piL} implies high modulation efficiency). Although modulation efficiency can be reduced further by increasing free-carrier densities of the PN junction, it results in high optical loss due to free-carrier absorption.¹² In these terms, LSPN can provide larger modulation efficiency, maintaining optical loss due to the larger mode overlap between optical mode and larger junction area of LSPN compared to LPN,^{14–18} but the larger junction area increases the junction capacitance, limiting the modulation speed. Although LSPN devices have been demonstrated, there have been no reports that provide a systematic and quantitative device performance comparison between LPN and LSPN optical phase shifters for the important device parameters of modulation efficiency, optical loss, and bandwidth. Therefore, it is important in the design

of LSPN-based optical phase shifters to consider not only the static performance of V_{piL} and optical phase shifter loss but also the intrinsic RC time constant of the active regions. In addition, we used the phase shifter loss as an x -axis to compare other performance parameters of the two devices. The performance parameters are highly dependent on the free-carrier densities of the PN junction, which is mainly determined by the dose amount. However, since the two-dimensional doping profiles are different and their nominal values cannot be representative and compared, it is more appropriate to use the phase shifter loss rather than the doping concentration or dose density as an x -axis.

In this study, we first introduce an easy fabrication method of LSPN by using overlapped-area ion implantation to invert the dominant dopant type in Si using an available process of Si photonics foundry services. Then, we present and discuss the simulated device performance of both Si optical phase shifters. Finally, we present the feasibility of 50 Gbps NRZ-OOK operation using Si LSPN-lumped MZ modulators.

2. Device structure

Figures 1(a) and 1(b) show the cross-sectional device structures of the Si LPN and LSPN optical phase shifters, respectively. The devices can be fabricated using conventionally available Si photonics foundry services. The Si waveguide width (w) is 450 nm designed for the C band. The mesa is 160 nm and the Si slab thickness is 60 nm. Si regions are p -type or n -type doped, and their doping levels are very heavy (p^{++} -Si and n^{++} -Si, $\sim 10^{20}$ cm⁻³) for ohmic contact, heavy (p^+ -Si and n^+ -Si, $\sim 10^{19}$ cm⁻³) for low series resistance, and light (p -Si and n -Si, ~ 0.2 to $\sim 1.0 \times 10^{18}$ cm⁻³ depending on dose conditions) for optical phase shift. As shown in the figures, NetActive shows free-carrier concentrations and the number of electrons (positive number) and holes (negative number), and PN junctions are clearly shown within the Si rib waveguides.

Table I shows the ion implantation conditions for the LPN and LSPN junction formation. The LPN is formed by two implantation steps for each phosphorus and boron atom with



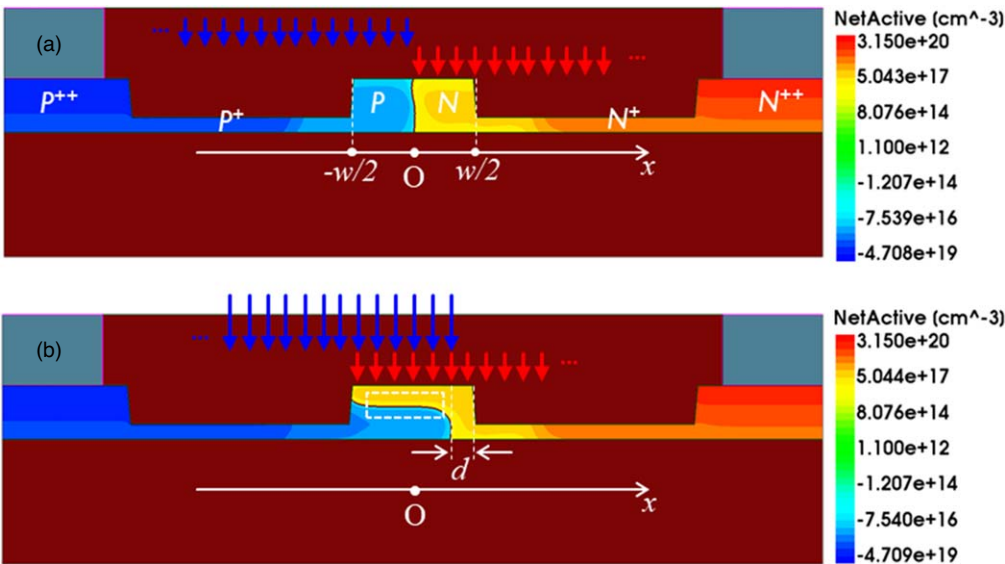


Fig. 1. (Color online) Cross-sectional carrier depletion-type optical phase shifters with (a) a lateral PN junction (LPN) and (b) an L-shaped PN junction (LSPN). NetActive indicates electron and hole concentrations for positive and negative numbers, respectively.

Table 1. Boron and phosphorus implantation conditions for LPN and LSPN optical phase shifters.

	Boron		Phosphorus	
	Dose ($1 \times 10^{13} \text{ cm}^{-2}$)	Energy (keV)	Dose ($1 \times 10^{13} \text{ cm}^{-2}$)	Energy (keV)
LPN	n	28	n	75
	n	45	n	135
LSPN	2n	35	n	30
	2n	45	n	80
			n	135

two different implantation energies and the same dose amount. The implantation areas are from the center of the Si waveguide to n^{++} -Si and p^{++} -Si sides, respectively. The LSPN is formed by triple phosphorus implantation followed by double Boron implantation. The implantation areas are from the left-hand edge of the red arrows ($-w/2$) to the n^{++} -Si side for phosphorus and from the right-hand side blue arrows ($w/2-d$) for boron. Here, d is the distance between the right-hand edge of the Si waveguide and the right-hand edge of the boron implantation region. Importantly, the dose amount for Boron is twice as large as that of phosphorus so that the doping type can be changed to p -type from n -type after boron implantation with a larger dose amount. In addition, it is noticeable that there is no significant cost issue in forming LSPN because only one more ion implantation step for boron is required and no additional masks are required compared to the LPN formation. The implantation energies are optimized to form the boundary of PN junction in the white dashed rectangle in Fig. 1(b) as horizontally as possible considering V_{piL} , phase shifter loss and cutoff frequency, and this greatly contributes optical phase shift. First, the three energies of phosphorus are chosen for peak densities to be uniformly positioned along the vertical direction in the rib waveguide, perpendicular to x -axis. Then, the two energies of boron with a twice as large dose are designed in such way to minimize the product of V_{piL} and loss but with a larger cutoff frequency than 30 GHz. Since the holes in Si are shown to be highly effective and

have less loss,⁸⁾ a more efficient structure design would be arranging n -Si for the top and p -Si for the bottom than the opposite way.^{19–21)} Therefore, this would result in a lower V_{piL} and phase shifter loss. In detail, the common conditions are a 7-degree tilt angle with four 90-degree rotations and a 5 nm screening SiO_2 layer on the top of Si waveguides for ion implantation. After the ion implantation process of other regions is completed, rapid thermal annealing for dopant activation is implemented at 1050 °C for 5 s.

3. Simulation result and discussion

To simulate the optical characteristics of modulators, Synopsys TCAD Sentaurus to calculate the carrier concentration and Lumerical optical mode solver for optical waveguides were used. The carrier concentration was calculated as a function of the applied DC reverse bias between the contact regions on the p^{++} - and n^{++} -Si. To simulate the optical characteristics, Soref’s model for the changes in the refractive index and absorption coefficient in Si was used.^{8,9)} The changes in the effective refractive index and absorption coefficient in the modulators are extracted by using the optical mode solver with the model. Details on our simulation method, which has been well calibrated and verified, can be found in.^{18,22,23)} We implemented this simulation at the variable dose conditions of $n = 0.5$ to 1.6 with 0.1 steps in Table 1. Figure 2 shows the electro-optical phase shifter performance of the LPN and LSPN optical phase shifters. Figure 2(a) shows V_{piL} as a function of the phase shifter loss at 0 V under all dose conditions. The passive loss of 1.5 dB cm^{-1} is added to the optical phase shifter loss since only free-carrier absorption is included in TCAD simulation. As the dose increases, the number of free carriers increase, and so the phase shifter loss increases and V_{piL} decreases. We chose two conditions among them that are almost the same as the phase shifter loss near 10.5 dB cm^{-1} for a reasonable comparison of their change in effective refractive index (Δn_{eff}) dependent on the bias voltage. This is because the change is highly dependent on the loss, and thus doping density. Figure 2(b) presents Δn_{eff} as a function of bias

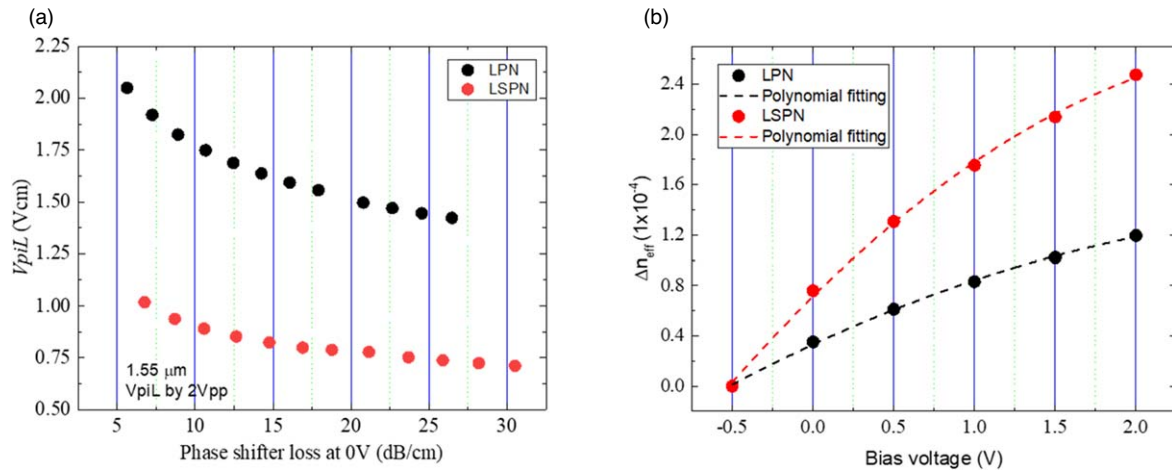


Fig. 2. (Color online) Electro-optical phase shifter performance of LPN and LSPN optical phase shifters: (a) modulation efficiency ($V_{pi}L$) as a function of phase shifter loss at 0 V, (b) change in effective refractive index as a function of bias voltage at the phase shifter loss near 10 dB cm⁻¹.

voltage at the loss near 10.5 dB cm⁻¹. The second-order polynomial fitting results are also plotted and will be used for large-signal simulation later. Since the Δn_{eff} and optical phase shifter loss are in a tradeoff relationship, we compared them at the almost same loss. LSPN shows much higher Δn_{eff} due to a larger overlap between the optical mode and PN junction compared to LPN. This might lead to over-estimation of device performance when $V_{pi}L$ is estimated using near 0 V, such as -0.5 to 0 V or 0 to 0.5 V because the slope of Δn_{eff} becomes lower as the reverse bias increases. Also, modulators practically operate at large-signal voltages, e.g. 2 V_{peak-to-peak}. Therefore, $V_{pi}L$ in this study is based on the phase shift differences between 0 and 2 V of the large-signal voltages. It is expressed as follows:

$$V_{pi}L = \pi L \frac{\Delta V}{\Delta \varphi} = \frac{\lambda}{2} \frac{\Delta V}{\Delta n_{eff}} = \frac{\lambda}{2} \frac{(2 \text{ V})}{(n_{eff} \text{ at } V = -2 \text{ V} - n_{eff} \text{ at } V = 0 \text{ V})}, \quad (1)$$

where L is the phase shifter length, φ is the phase shifter, and λ is the wavelength.

It is shown that $V_{pi}L$ values for LSPN are much smaller than that for LPN in all dose conditions. In particular, $V_{pi}L$ for LSPN at 10.5 dB cm⁻¹ is 0.89 Vcm while that of LPN at 10.5 dB cm⁻¹ is 1.76 Vcm, indicating that modulation efficiency is nearly doubled by using LSPN at the same loss. In addition, the figure-of-merit for the modulator of the product of the phase shifter loss and $V_{pi}L$ ($\alpha V_{pi}L$) is ~ 9.3 VdB and ~ 18.5 VdB, respectively. It is reasonable to compare two devices at the same loss because $\alpha V_{pi}L$ is lower for lightly doped cases, compared to highly doped cases, depending on the loss.¹⁸⁾

Figure 3 shows the electrical characteristics of the LPN and LSPN optical phase shifters. The simulated series resistance (R_s) and junction capacitance (C_j) across cathode and anode electrodes as a function of the phase shifter loss are shown in Figs. 3(a) and 3(b), respectively. As the loss increases, the series resistance decreases but junction capacitance increases due to an increase in the free-carrier density. When the reverse bias voltage of -2 V is applied, the C_j of LSPN decreases much larger than that of LPN, leading to a

much more efficient modulation efficiency. However, mainly due to the large C_j , the cutoff frequency (f_{cutoff}) of LSPN is smaller than that of LPN, which is calculated by $f_{cutoff} = 1/(2\pi R_s C_j)$.¹³⁾ As C_j decreases by applying a reverse bias voltage, f_{cutoff} increases. For LSPN, this is smaller than that of LPN, but it is still larger than 30 GHz.

Figure 4 shows the d dependency on $V_{pi}L$ and f_{cutoff} as a function of the phase shifter loss. Here, f_{cutoff} at 0 V is only plotted because it is lower than that at -2 V due to the larger C_j , and the dynamic performance is limited by the lower f_{cutoff} . For LSPN, it is possible to adjust $V_{pi}L$ and f_{cutoff} because the C_j is adjusted by the design parameter, d . With an increase of d , $V_{pi}L$ decreases and f_{cutoff} increases owing to the decrease in C_j . When d is 150 nm, the f_{cutoff} is larger than 35 GHz, which enables the 50 Gbps NRZ data rate.^{24,25)}

Since the main drawback of LSPN is the smaller f_{cutoff} due to the larger C_j compared to that of LPN, one could compensate by using a single-drive configuration, reported in,²⁶⁾ shown in Fig. 5(a). Figures 5(b) and 5(c) show equivalent circuit models of single-drive (SD) and a half part of double-drive (DD) configurations for two phase shifters at both arms. Compared to the double-drive configuration, the two capacitances are connected in series for the single-drive configuration, so the C_j can be reduced by a half.

For the quantitative analysis, we used the open-source electronic circuit simulator, Ngspice²⁷⁾ for small- and large-signal responses. To verify our dynamic simulation methods, we first use this method to reproduce the reported results of S21 in the literature.^{26,28)} Experimental values from the literature²⁸⁾ were used: $C_0 = 26$ fF, $L = 0.176$ nH, $R_s = 12.7$ Ω and $C_j = 0.26$ pF. After the verification, we continue to use the values of C_0 and L while R_s and C_j are given by our simulation for different structures and fabrication conditions. Although C_0 and L are not as dominant as R_s and C_j , it is important to use reasonable and realistic value. Therefore, we used the experimentally reported values for C_0 and L . Also, such a method was previously reported in the literature.²⁶⁾ Our simulated 3 dB bandwidths of SD and DD are 11 and 19 GHz based on the SPICE, while the literature²⁸⁾ shows 10.7 and 18 GHz, presenting a good agreement with our method.

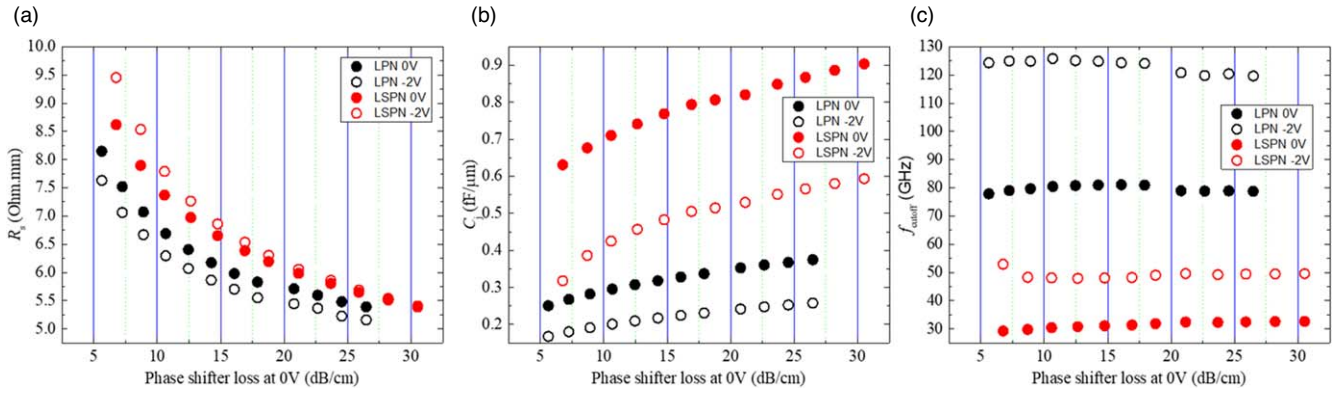


Fig. 3. (Color online) Electrical characteristics for LPN and LSPN optical phase shifters: (a) series resistance, (b) junction capacitance, and (c) cutoff frequency based on the intrinsic RC time constant of the active region.

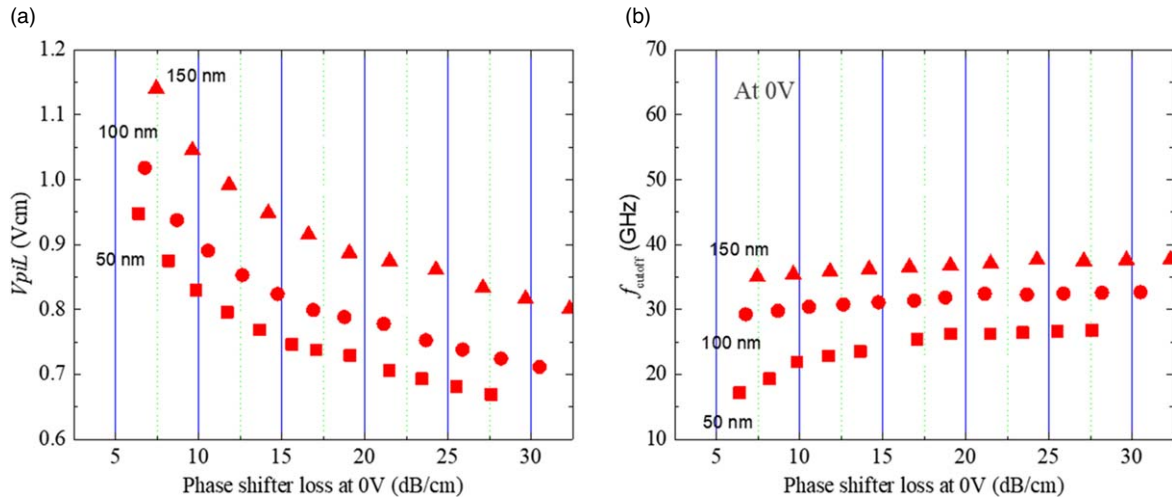


Fig. 4. (Color online) d dependency of (a) V_{piL} and (b) cutoff frequency as a function of phase shifter loss.

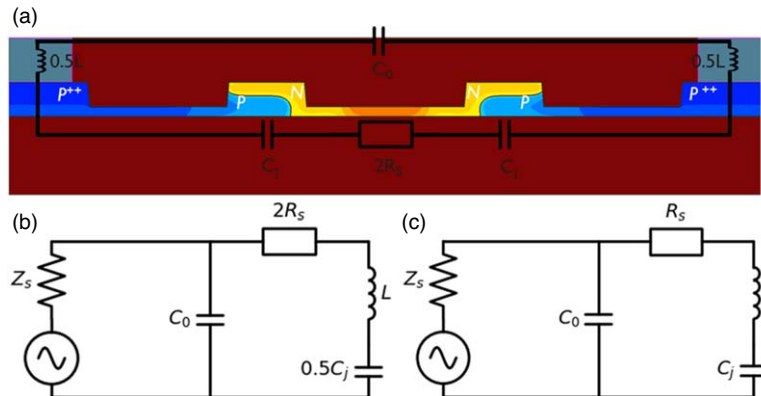


Fig. 5. (Color online) (a) Schematic of single-drive configuration and equivalent circuit models of (b) single-drive (SD) and (c) a half part of double-drive (DD) configurations.

Figure 6 shows the small-signal responses of S21 at 0 and -2 V for different input impedances. Both LPN and LSPN correspond to the devices in Fig. 1(a), in which the phase shifter losses are same. If a specially designed low Z_s IC driver is used, this limitation can be eliminated^{29,30} and RLC-limited performance will be dominant.²⁶ As expected, the LPN shows larger 3 dB bandwidths than LSPN. Since C_j is dominant for the S21, the 3 dB bandwidths increase when a reverse bias is applied and when SD is used instead of DD. In particular, the 3 dB bandwidth is improved by reducing Z_s .

As a result, the LSPN with a SD configuration shows a 3 dB bandwidth up to 26 GHz.

In addition, we implemented a large-signal simulation using the same two devices at the same loss, and the simulated 50 Gbps eye diagrams are shown in Fig. 7. The second-order polynomial-fitted functions of the bias-dependent Δn_{eff} , R_s , and C_j are used for large-signal modeling. The input optical power is assumed to be 1 mW and the input signal is PRBS $2^7 - 1$ pattern with 4 V_{peak-to-peak} without any pre-emphasis. For LPN, as predicted by the S21 results, the largest eye-opening is estimated to be 0.12 mW when $Z_s = 25$

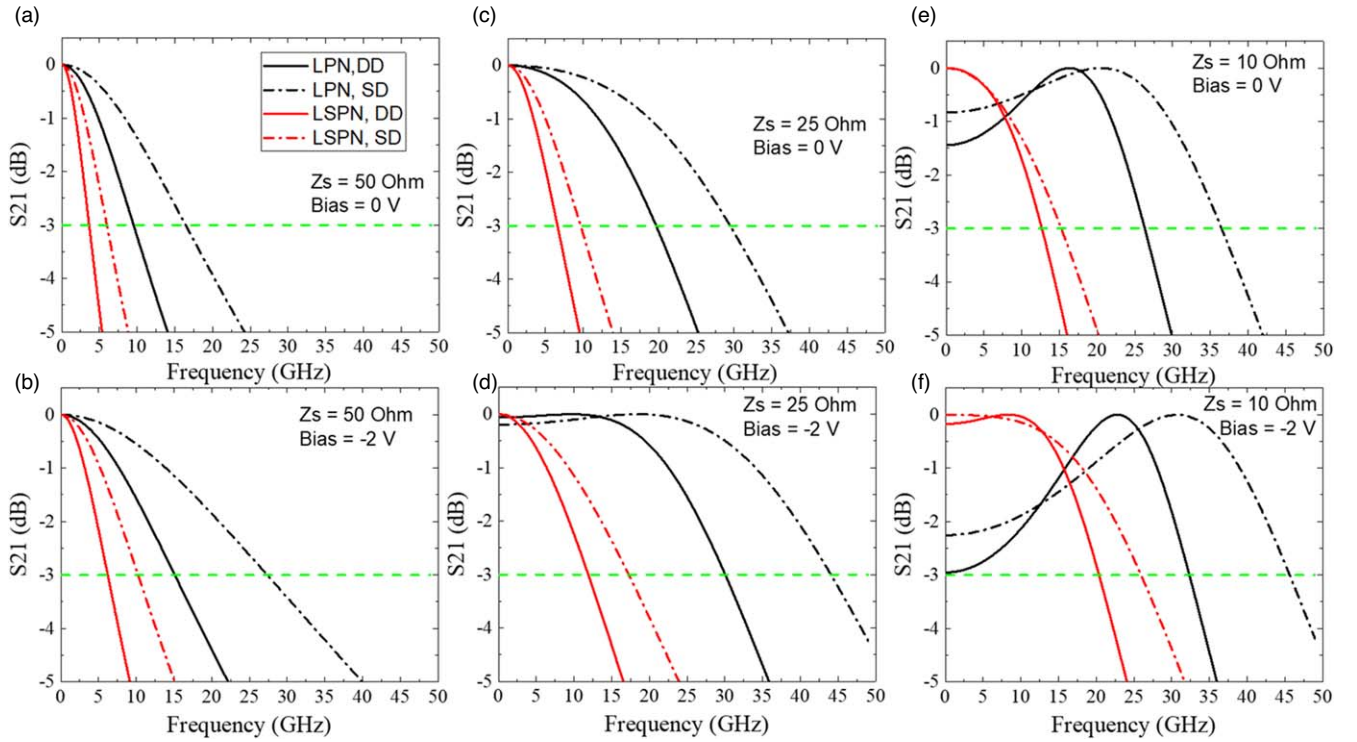


Fig. 6. (Color online) Small-signal response at 0 and -2 V for (a) and (b) $Z_s = 50$ Ω , (c) and (d) $Z_s = 25$ Ω , and (e) and (f) $Z_s = 10$ Ω .

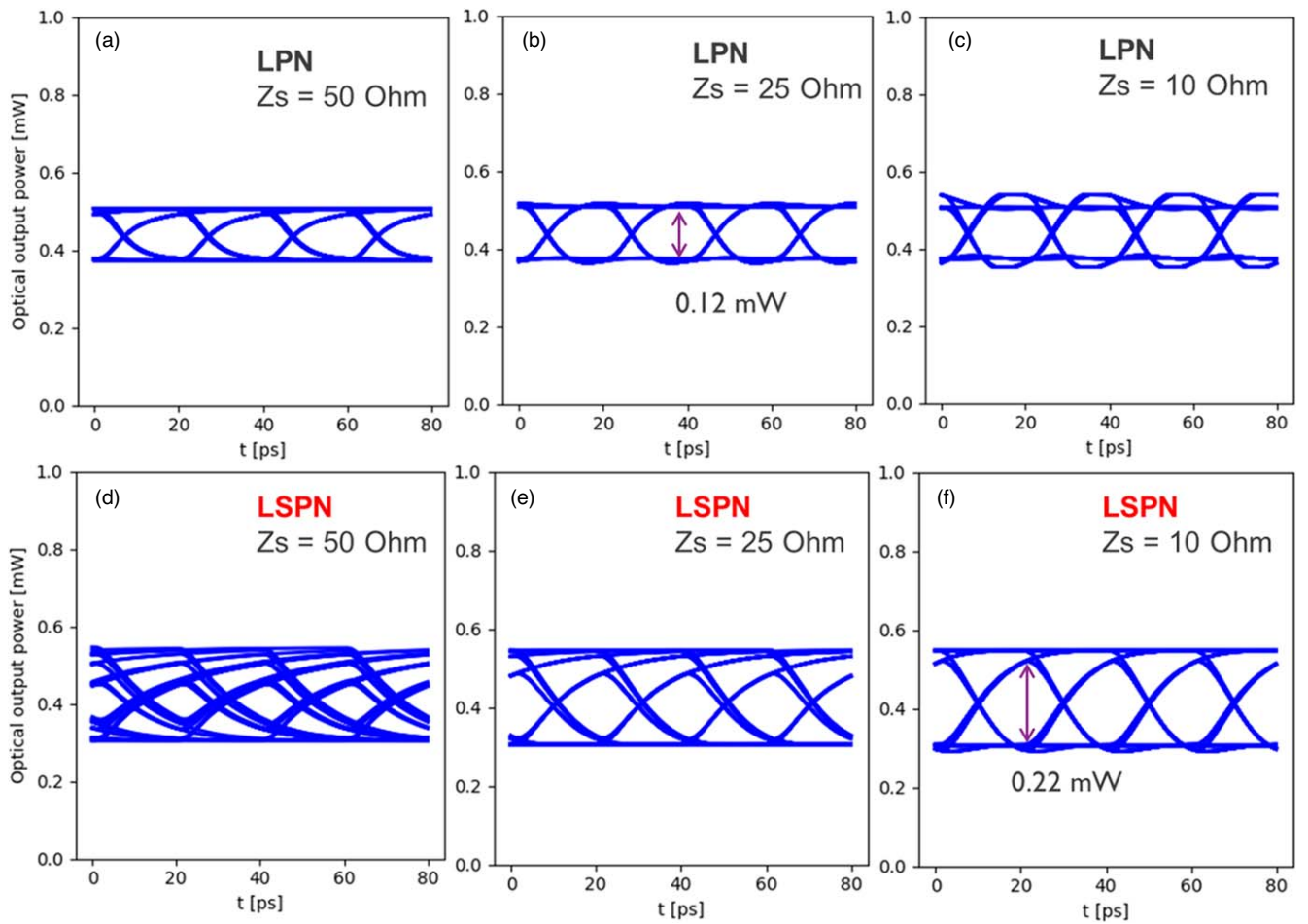


Fig. 7. (Color online) Simulated eye diagrams for 50 Gbps with a $2^7 - 1$ pattern of SD configuration-based LPN for (a), (b), and (c) and LSPN for (d), (e), and (f) with different input impedances, $Z_s = 50$ Ω , 25 Ω , and 10 Ω , respectively.

Ω . The speed is limited when Z_s is too high ($Z_s = 50 \Omega$) and unnecessary peaking is seen when Z_s is too low ($Z_s = 10 \Omega$). Regarding the time-domain peaking in Fig. 7(c), it corresponds to the frequency-domain peaking, $f_{peaking}$ of S21 for LPN, SD, shown in Figs. 6(e) and 6(f). As Z_s becomes smaller, the signal loss becomes smaller too. Thus, the peaking mainly caused by L and C_j appears near where it already exists in the range of 31 to 38 GHz ($f_{peaking} \simeq 1/2\pi(LC_j)^{0.5}$). For LSPN, both cases of $Z_s = 25$ and 50Ω show speed-limited eye diagrams, meaning total impedance is necessary to be reduced further. With a decrease in Z_s , the eye diagram becomes much larger and the eye-opening is 0.22 mW ($Z_s = 10 \Omega$) which is 1.8 times larger than LPN. The eye diagram of LSPN might not be enough for error-free operation due to the limited EO response. However, it is possible for LSPN to use d to increase the EO response sacrificing modulation efficiency, as discussed in Fig. 4. Therefore, it will be important for the clearest eye diagram to optimize the LSPN design considering the tradeoff in a target optical link specification.

4. Conclusion

A comparative study of Si optical phase shifters with lateral and L-shaped PN junctions was conducted by TCAD simulation. We show an easy-to-follow fabrication method for L-shaped PN junctions and the static device performance of both Si optical phase shifters. The L-shaped PN junction Si optical phase shifter shows much greater modulation efficiency of V_{piL} and lower optical phase shifter loss compared to the lateral one. Also, the large-signal simulation shows a dynamic optical modulation amplitude of 0.22 mW for the vertical one, which could offer a promising solution for a compact device footprint without a traveling wave electrode.

Acknowledgments

This work was supported by the research fund of Hanyang University (HY-2020-2750).

ORCID iDs

Younghyun Kim  <https://orcid.org/0000-0001-8072-1251>

- 1) D. J. Thomson et al., *IEEE Photonics Technol. Lett.* **24**, 234 (2012).
- 2) P. Dong, L. Chen, and Y. Chen, *Opt. Express* **20**, 6163 (2012).
- 3) P. Dong et al., *Opt. Express* **17**, 22484 (2009).

- 4) G. T. Reed, G. Z. Mashanovich, F. Y. Gardes, M. Nedeljkovic, Y. Hu, D. J. Thomson, K. Li, P. R. Wilson, S. W. Chen, and S. S. Hsu, *Nanophotonics* **3**, 229 (2014).
- 5) G. T. Reed, D. J. Thomson, F. Y. Gardes, Y. Hu, J. M. Fedeli, and G. Z. Mashanovich, *Front. Phys.* **2**, 1 (2014).
- 6) C. Xiong, D. M. Gill, J. E. Proesel, J. S. Orcutt, W. Haensch, and W. M. J. Green, *Optica* **3**, 1060 (2016).
- 7) P. Dong, X. Liu, S. Chandrasekhar, L. L. Buhl, R. Aroca, and Y. K. Chen, *IEEE J. Sel. Top. Quantum Electron.* **20**, 6100108 (2014).
- 8) R. A. Soref and B. R. Bennett, *IEEE J. Quantum Electron.* **23**, 123 (1987).
- 9) M. Nedeljkovic, R. Soref, and G. Z. Mashanovich, *IEEE Photonics J.* **3**, 1171 (2011).
- 10) R. Ding et al., *Opt. Commun.* **321**, 124 (2014).
- 11) M. Streshinsky et al., *Opt. Express* **21**, 30350 (2013).
- 12) K. Ogawa et al., *IEICE Electron. Express* **11**, 20142010 (2014).
- 13) J. Van Campenhout et al., 2018 Optical Fiber Communications Conf. and Exposition (OFC), 2018W11.1.
- 14) M. R. Watts, W. A. Zortman, D. C. Trotter, R. W. Young, and A. L. Lentine, *IEEE J. Sel. Top. Quantum Electron.* **16**, 159 (2010).
- 15) M. R. Watts, W. A. Zortman, D. C. Trotter, R. W. Young, and A. L. Lentine, *Opt. Express* **19**, 21989 (2011).
- 16) Y. Maegami, G. Cong, M. Ohno, M. Okano, K. Itoh, N. Nishiyama, S. Arai, and K. Yamada, *Opt. Express* **25**, 31407 (2017).
- 17) C. E. Png, T. Y. L. Ang, J. R. Ong, and S. T. Lim, *Proc. SPIE* **10537**, 105370H (2018).
- 18) Y. Kim, M. Takenaka, and S. Takagi, *IEEE J. Quantum Electron.* **51**, 5200107 (2015).
- 19) J. Sun, M. Sakib, J. Driscoll, R. Kumar, H. Jayatilaka, Y. Chetrit, and H. Rong, 2018 Optical Fiber Communications Conf. and Exposition (OFC), 2018Th4A.7, 10.1364/OFC.2018.Th4A.7.
- 20) J. Chen, L. Zhou, G. Zhou, Y. Zhou, Y. Zhong, S. Liu, Y. Guo, and L. Liu, *Proc. SPIE* **10964**, 1096419 (2018).
- 21) C. E. Png, T. Y. L. Ang, J. R. Ong, and S. T. Lim, *Proc. SPIE* **10537**, 105370H (2018).
- 22) Y. Kim, S. Kim, Y. Ban, S. Lardenois, D. Yudistira, M. Pantouvaki, and J. Van Campenhout, 2019 IEEE 16th Int. Conf. on Group IV Photonics (GFP), 2019WP29.
- 23) S. Kim, Y. Kim, Y. Ban, M. Pantouvaki, and J. Van Campenhout, *IEEE J. Quantum Electron.* **56**, 6300208 (2020).
- 24) Y. Kim, Y. Jo, M. Kim, B. M. Yu, C. Mai, S. Lischke, L. Zimmermann, and W. Y. Choi, *Jpn. J. Appl. Phys.* **58**, 062006 (2019).
- 25) "NRZ bandwidth (−3 dB HF cutoff vs SNR) how much bandwidth is enough?," Technical Report 02XXX-WTP-001-A Mindspeed Technologies, 2003, [www.semanticscholar.org/paper/NRZ-Bandwidth-\(-3-dB-HF-Cutoff-vs-SNR-\)-How-Much-is/c22e5a1ca2f4355195d0deb49546-bac78210d828](http://www.semanticscholar.org/paper/NRZ-Bandwidth-(-3-dB-HF-Cutoff-vs-SNR-)-How-Much-is/c22e5a1ca2f4355195d0deb49546-bac78210d828).
- 26) X. Li, F. Yang, F. Zhong, Q. Deng, J. Michel, and Z. Zhou, *Photonics Res* **5**, 134 (2017).
- 27) Ngspice: [<http://ngspice.sourceforge.net/>].
- 28) H. Yu et al., *Opt. Express* **20**, 12926 (2012).
- 29) M. Webster, K. Lakshmikummar, C. Appel, C. Muzio, B. Dama, and K. Shastri, *Conf. on Optical Fiber Communication, Technical Digest Series, June*, 20152015, 10.1364/OFC.2015.W4H.3.
- 30) D. Patel, V. Veerasubramanian, S. Ghosh, A. Samani, Q. Zhong, and D. V. Plant, *Opt. Express* **22**, 26788 (2014).